

Bayesian inference of PolII dynamics over the exclusion process.

Massimo Cavallaro,^{1,2,3,*} Yuexuan Wang,⁴ Daniel Hebenstreit,² and Ritabrata Dutta⁵

¹Mathematics Institute, University of Warwick, Coventry, UK

²School of Life Sciences, University of Warwick, Coventry, UK

³Zeeman Institute for Systems Biology and Infectious Disease Epidemiology Research, University of Warwick, Coventry, UK

⁴Institute of Applied Statistics, Johannes Kepler Universität, Linz, Austria

⁵Department of Statistics, University of Warwick, Coventry, UK

Transcription is a complex phenomenon that permits the conversion of genetic information into phenotype by means of an enzyme called PolII, which erratically moves along and scans the DNA template. We perform Bayesian inference over a paradigmatic mechanistic model of non-equilibrium statistical physics, i.e., the asymmetric exclusion processes in the hydrodynamic limit, assuming a Gaussian process prior for the PolII progression rate as a latent variable. Our framework allows us to infer the speed of PolIIs during transcription given their spatial distribution, whilst avoiding the explicit inversion of the system's dynamics. The results may have implications for the understanding of gene expression.

I. INTRODUCTION

The DNA is a long polymeric molecule that encodes information as a sequence of nucleotides (Nts). Turning this information into a phenotype is a complex phenomenon hinged upon transcription, the molecular process in which particular segments of DNA (i.e., the genes) are scanned and their information is copied into mRNA by the enzyme RNA polymerase II (PolII). The transcription itself consists of several steps which can be differentially regulated to alter the timing and the output of the mRNA production [1, 2].

The transcription can also be seen as a non-equilibrium process, where the PolIIs are being transported as particles on a one dimensional lattice, the lattice being the DNA template which the PolIIs bind to. We can further consider this process having left and right boundaries, representing the transcription start site (TSS) and the transcription end site (TES), respectively (Fig. 1 A). Within the gene body, the PolIIs erratically travel along the template and their abrupt slowing down in certain genomic regions is known as the *pausing* dynamics [3, 4]. While the pausing is an essential part of the transcriptional machinery and contributes to the regulation of genes' expression levels, a comprehensive quantitative understanding of its dynamics is still missing [5, 6].

To help understand gene regulation, we present here a framework to quantitatively study the pausing dynamics. We model these by means of a generalisation of a paradigmatic model of transport, the asymmetric simple exclusion process (ASEP, [7]) in the hydrodynamic limit [8]. The behaviour of this model is chiefly determined by the rates at which the particles hop on the lattice, with the lowest rates corresponding to pausing regions. More specifically we require the rate profile function, which we refer to as \tilde{p} , to be spatially varying yet smooth as in references [9, 10], thus making it possible

to model this function by a Gaussian process (GP) [11]. Noticing the analogy between the PolII transport in the gene body and the particle hopping in the exclusion process, learning \tilde{p} allows the study of the pausing dynamics in a gene. We provide an inferential scheme to learn this rate function by Bayesian inference assuming a prior on the profile function induced by a GP prior on a latent variable. In other words, integrating the dynamics defined by \tilde{p} generates transient density profiles; we aim at estimating \tilde{p} given observed density profiles without explicitly inverting the system's dynamics. Due to its generality, our framework can be deployed to estimate the rate profiles of any one-dimensional transport problem.

The manuscript is organised as follows. Section II A describes the biology of pausing and the next-generation sequencing (NGS) data types which are available to study it. Section II B and II C, respectively, discuss the asymmetric simple exclusion process as a mathematical model for transcription with pausing and a Bayesian inferential framework for model fitting. We present the results in section III and conclude with a discussion in section IV.

II. MODEL DEFINITION

A. Biological processes and data

The enzyme PolII has a central role in the biology of transcription. In order to catalyse synthesis of the mRNA, it binds to the DNA upstream the TSS, initiates the mRNA synthesis, and then traverses the DNA downstream (elongation) until it pauses at a certain gene location, ready to respond to a developmental or environmental signal that instructs to resume the elongation. The process terminates when the PolII reaches the TES and the transcribed mRNA is released. As a result of these steps, the output is modulated in both timing and intensity. However, many details, such as the pausing, are not well understood [5]. The presence of transcriptional pausing is revealed by several assays based

* m.cavallaro@warwick.ac.uk

on NGS, which is widely used in molecular biology to study molecules involved in genic processes. In the PolII *ChIP-seq* assay, PolII-bound DNA is isolated by chromatin immunoprecipitation with a PolII antibody and is then subject to high-throughput sequencing. This provides a genome-wide view of the PolII binding sites for all forms of PolII, including both those poised or transcriptionally engaged and those which are bound to DNA and static. For each genomic position, PolII ChIP-seq returns a signal when the position is found occupied by a polymerase.

For this study, we binned ChIP-seq reads from genomic ranges of selected genes (*Materials and Methods*) into 20-Nt bins, thus yielding coarse-grained read profiles (which we refer to as y) such as those illustrated in Fig. 1 B. The number of these reads at a position x is proportional to the occupation probability $\varrho(x)$. The proportionality factor, which depends on the number of cells used in the experiment and on further signal amplification intrinsic to the sequencing procedure, cannot be directly accessed with precision and is only known with substantial uncertainty [12].

Other methods available to study the pausing include but are not limited to *NET-seq*, where nascent mRNA chunks associated with immunoprecipitated PolII complexes are isolated and sequenced [13], *GRO-seq*, where RNAs recently transcribed only by transcriptionally-engaged PolIIs are sequenced [14], and *PRO-seq*, which is similar to GRO-seq but reaches single-nucleotide resolution [15]. The evidences of PolII transport are particularly clear in time-course experiments, where sequencing data are collected over time following a perturbation. As an example, time-variant PRO-seq has been suggested to estimate pausing times in key peak regions [16]. A classical way to perturb these molecular dynamics is inhibiting the initiation by treating the cells with triptolide (Trp) [17, 18]. This permits the PolII already engaged in transcription to progress further downstream the gene while new PolIIs are prevented to attach, thus freeing upstream genomic regions as the run-on time progresses (Fig. 1 C). Our approach consists of using the read profiles y as functions of x , collected at fixed run-on times t_1 , t_2 , t_3 , and t_4 after treatment, to infer the dynamics. While Trp inhibits new initiation, poised PolII upstream the TSS can still pass through it, enter the gene template, and perform elongation immediately after Trp treatment [17, 18]. To account for this, we also perform inference over Spt5 ChIP-seq data, where the poised polymerases are masked while those bound are detected [18].

These types of experiments reveal the presence of a flux of PolIIs, which is the signature of the non-equilibrium physics involved in the elongation process. The profile y^* observed prior to the treatment corresponds to a non-equilibrium stationary state (NESS). Disrupting initiation with Trp yields a transient state, which evolves from y^* until it settles down to a new NESS.

B. Mathematical model

The transport of particles on a one dimensional lattice is a well-studied problem in mathematics and physics. Its basic features are captured by the asymmetric simple exclusion process (ASEP) [7], which defines the stochastic dynamics of interacting particles on a discrete lattice, which we take here to be a one-dimensional chain with open boundary conditions. Let the total number of lattice sites be N . The state of each site i , $1 \leq i \leq N$, is characterized by the occupation number n_i such that $n_i = 0$ if the site is empty and $n_i = 1$ if it is occupied by a particle. The evolution proceeds in continuous time. A particle on site $i < N$ hops rightward into the site $i + 1$ with rate p_i , the transition being successful only if the site $i + 1$ is empty. Similarly, a particle on site $i > 1$ hops leftward into $i - 1$ with rate q_i , if the site $i - 1$ is empty. Further, particles on the left (right) boundary site $i = 1$ ($i = N$) leave the lattice at rate q_0 (p_N), while particles are injected in the same boundary site at rate p_0 (q_N) if the site is empty. The constraint that a jump can occur only if the target is empty prevents the accumulation of more than one particle on a site and is generically referred to as the exclusion rule. This rule allows particle collision, which causes congestion when the particle density is sufficiently high and permits phase transitions between a low density, high density, and a maximum current phase even if the systems is one dimensional [19]. Interestingly, it has been suggested that PolII congestion is important in transcription [20].

While the ASEP was originally proposed to model biopolymerization on DNA [21], this and related models have been applied to diverse problems, e.g., protein translation [22–24], molecular motors [25], pedestrian and vehicle traffic [26]. Recently proposed applications to transcription incorporate disordered dynamics [27]. ASEP’s theoretical appeal is due to its analytical results representative of a large class of models [28, 29] and a convenient mean-field treatment that yields the exact stationary solution [30]. In the context of transcription, particles entering site 1, moving along the chain, and exiting at site N correspond to initiation, elongation, and termination, respectively. The lowest values of p_i model the presence of obstacles which hinder the movement and represent the pausing sites in the gene. Other substantial models of transcriptional dynamics do not fully capture these properties [31–33].

The dynamics of the expected occupation of a single site i in the bulk are governed by the lattice continuity equation

$$\frac{d}{dt}\mathbb{E}(n_i(t)) = J^{\text{left}}(t) - J^{\text{right}}(t), \quad (1)$$

$0 < i < N$, where \mathbb{E} denotes expectation value and $J^{\text{left}}(t)$ and $J^{\text{right}}(t)$ are the average flux of particles from site $i - 1$ to site i and from site i to site $i + 1$, respectively.

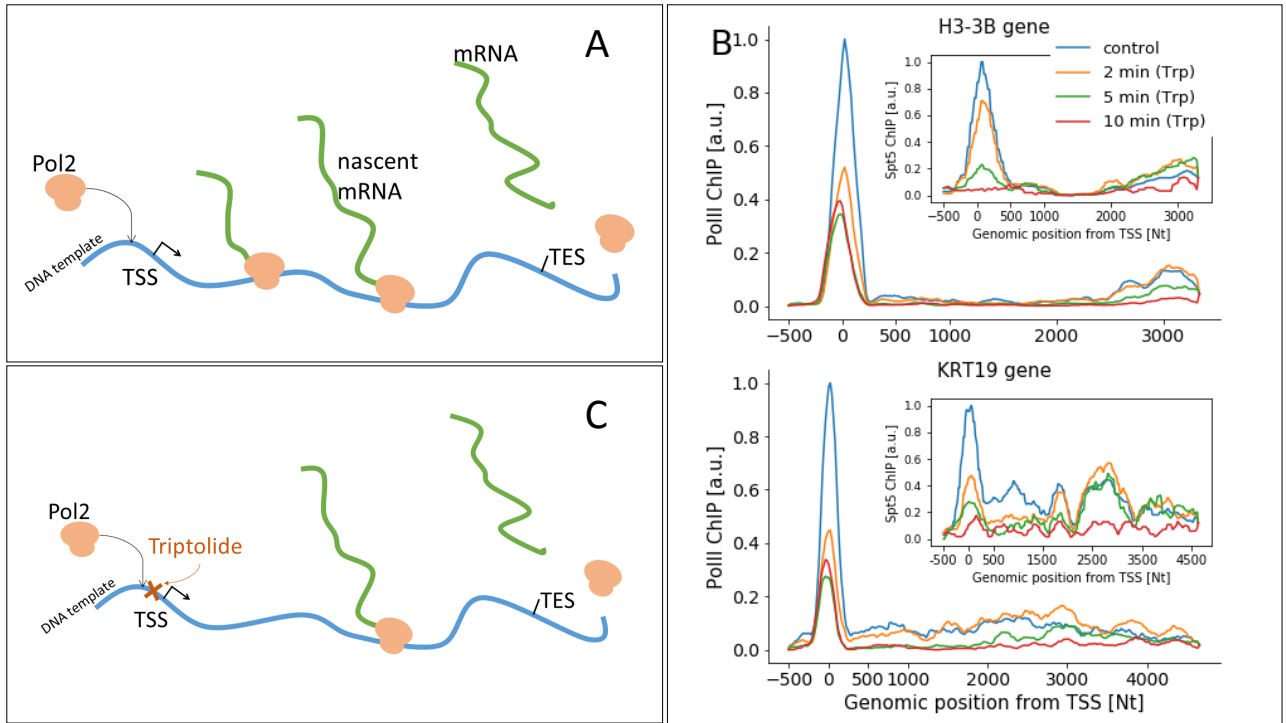


FIG. 1. Biological process and data. A) Simplified diagram of mRNA synthesis. PolII molecules bind to the DNA upstream of transcription start site (TSS) and moves downstream towards the transcription end site (TES), where it is released along with the synthesized mRNA. B) ChIP-seq experiments yield the relative abundance of PolII at each genomic position, here illustrated for H3-3B (top) and KR19 genes (bottom); insets show the Spt5-bound PolII abundances for the same genes. C) In the presence of triptolide, transport is blocked upstream of TSS, while transcriptional engaged PolII are allowed to complete elongation; this is reflected in the ChIP-seq profiles obtained 2, 5, and 10 minutes after treatment (also in B).

These are subject to the exclusion rule and therefore obey

$$\begin{aligned}
 J^{\text{left}}(t) &= p_{i-1} \mathbb{E}(n_{i-1}(t)(1 - n_i(t))) \\
 &\quad - q_i \mathbb{E}(n_i(t)(1 - n_{i-1}(t))), \\
 J^{\text{right}}(t) &= p_i \mathbb{E}(n_i(t)(1 - n_{i+1}(t))) \\
 &\quad - q_{i+1} \mathbb{E}(n_{i+1}(t)(1 - n_i(t))).
 \end{aligned} \tag{2}$$

In order to exactly solve these dynamics, second-order moments such as $\mathbb{E}(n_i(t)n_{i+1}(t))$ need to be known. Under independence assumption, these moments are factorised, which in our case amounts to replacing equations (1)–(2) with

$$\begin{aligned}
 \frac{d}{dt} \phi_i(t) &= p_{i-1} \phi_{i-1}(t)(1 - \phi_i(t)) - p_i \phi_i(t)(1 - \phi_{i+1}(t)) \\
 &\quad + q_{i+1} \phi_{i+1}(t)(1 - \phi_i(t)) - q_i \phi_i(t)(1 - \phi_{i-1}(t)),
 \end{aligned} \tag{3}$$

where we used $\phi_i(t) := \mathbb{E}(n_i(t))$ to lighten the notation. In other words, equations (3) define the so-called mean-field dynamics of the asymmetric exclusion process, which are known to approximate well the true dynamics in many contexts, predict crucial features such as dynamical phase-transitions, and ease mathematical treat-

ment [19, 30, 34]. With open boundaries,

$$\begin{aligned}
 \frac{d}{dt} \phi_1(t) &= p_0 (1 - \phi_1(t)) - p_1 \phi_1(t)(1 - \phi_2(t)) \\
 &\quad - q_0 \phi_1(t) + q_1 \phi_2(t)(1 - \phi_1(t)),
 \end{aligned} \tag{4}$$

$$\begin{aligned}
 \frac{d}{dt} \phi_N(t) &= p_{N-1} \phi_{N-1}(t)(1 - \phi_N(t)) - p_N \phi_N(t) \\
 &\quad + q_N (1 - \phi_N(t)) - q_{N-1} \phi_N(1 - \phi_{N-1}).
 \end{aligned} \tag{5}$$

To match the available data that is coarse grained (Fig. 1 B), instead of considering particles individually we rely on their hydrodynamics description, which is obtained as follows. We assume Euler scaling with constant a and let $a \rightarrow 0, N \rightarrow \infty$, with $L := Na$ held finite. We define the functions $\varrho : \mathbb{R}^2 \rightarrow \mathbb{R}_0^+$, $\tilde{p} : \mathbb{R} \rightarrow \mathbb{R}_0^+$, and $\tilde{q} : \mathbb{R} \rightarrow \mathbb{R}_0^+$ such that they are analytic and bounded on $]0, L[\times]0, \infty[$, $]0, L[$, and $]0, L[$, respectively, and

$$\begin{aligned}
 \phi_i(t) &= \varrho((i-1)a, t), \\
 p_i &= a \tilde{p}((i-1)a), \\
 q_i &= a \tilde{q}((i-1)a),
 \end{aligned} \tag{6}$$

we further assume that the left and right jump rates satisfy $\tilde{q}(x) = b \tilde{p}(x), \forall x \in [0, L]$, with $0 \leq b < 1$, where b governs the relative strength of the non-equilibrium driving forces. The case $b = 0$ corresponds to a *totally asymmetric exclusion process* (TASEP), while the limit case

$b = 1$ corresponds to the *symmetric exclusion process*. Intermediate values $0 < b < 1$ correspond to settings where the particles can jump in both directions, but are driven rightwards in average, as expected in molecular biology [35, 36]. A continuum-limit counterpart of equations (2), as derived in references [9, 10], is

$$J(x, t) = a\tilde{p}(x)\varrho(x - a/2, t)(1 - \varrho(x + a/2, t)) - a\tilde{q}(x)\varrho(x + a/2, t)(1 - \varrho(x - a/2, t)), \quad (7)$$

which, using first-order Taylor expansion, yields

$$J(x, t) \approx a(\tilde{p}(x) - \tilde{q}(x))\varrho(x, t)(1 - \varrho(x, t)) - \frac{a^2}{2}(\tilde{p}(x) + \tilde{q}(x))\frac{\partial}{\partial x}\varrho(x, t). \quad (8)$$

To lighten the mathematical notation, we define the two quantities

$$\begin{aligned} \lambda(x) &:= a(\tilde{p}(x) - \tilde{q}(x)) = a\tilde{p}(x)(1 - b), \\ \nu(x) &:= \frac{a^2}{2}(\tilde{p}(x) + \tilde{q}(x)) = \frac{a^2}{2}\tilde{p}(x)(1 + b); \end{aligned} \quad (9)$$

their ratio is constant in x , viz., $\nu(x)/\lambda(x) = a/2(1 + b)/(1 - b)$, which equals $a/2$ in the totally asymmetric case.

Substituting (8)–(9) into the continuity equation

$$\frac{\partial}{\partial t}\varrho(x, t) = -\frac{\partial}{\partial x}J(x, t), \quad (10)$$

which is the hydrodynamics limit of equation (1), gives the non-linear partial differential equation

$$\frac{\partial}{\partial t}\varrho(x, t) = -\frac{\partial}{\partial x}\left\{\lambda(x)\varrho(x, t)(1 - \varrho(x, t)) - \nu(x)\frac{\partial}{\partial x}\varrho(x, t)\right\}, \quad (11)$$

which can be linearised to

$$\frac{\partial}{\partial t}u(x, t) = \frac{\tilde{p}(x)}{2}\left\{a^2(1 + b)\frac{\partial^2}{\partial x^2}u(x, t) - \frac{(1 - b)^2}{1 + b}u(x, t)\right\} \quad (12)$$

by means of a generalisation of the Cole-Hopf transform (Appendix A and references [9, 37, 38]). For simplicity we set $(a, b) = (1, 0)$, arguing that our considerations remain valid with such a choice. The required boundary values $\varrho(0, t)$, $\varrho(L, t)$, and $\varrho(x, 0)$, and the numerical scheme used to integrate equation (12) are detailed in Appendices A and B.

Integrating equation (11) with boundary conditions analogous to equations (4)–(5) and initial density $\varrho(x, 0) > 0$ yields a NESS for large t , characterised by a non-vanishing average flux and a density profile $\varrho^*(x)$ which is invariant in time. Setting the latter as initial condition and further integrating with no inward particle

flux ($p_0 = q_N = 0$) produces a transient state that mimics the evolution of the PolII profile after Trp treatment until the density profile vanishes. This is illustrated, for a choice of boundary values and jump rate profile, in Fig. 2, which also includes the result of the inference process described in the next subsections.

C. Bayesian framework

We fit the model to real-world data by means of a Bayesian approach leveraging its ability to explicitly encode prior hypotheses about the quantities we wish to infer [39]. We are interested in the rate profile \tilde{p} . As this is required to be analytic and non-negative, it is convenient to assume a Gaussian process (GP) [11] functional prior on a latent variable f and induce a prior on \tilde{p} using a sigmoid link function $\tilde{p} = \tilde{p}_{\max}/(1 + \exp(-f))$, which further imposes an upper bound to \tilde{p} . The GP prior here defines a distribution over real valued C^1 functions in \mathbb{R} , where any finite set of function evaluations $f(x)$ has multivariate normal distribution with mean m and kernel $k(x, x'; \sigma_f^2, l) = \sigma_f^2 \exp(-(x - x')^2/(2l^2))$, $x, x' \in \mathbb{R}$.

The observations are organised into a collection of values $\mathbf{y} = \{y_{ij}\}_{ij}$, where the subscripts indicate that an observation is taken at position x_i and time t_j , $i = 1, 2, \dots, n$ and $j = 1, 2, \dots, t$. We assume that, in addition to the amplification factor introduced prior the sequencing procedure, the observed values include additive noise $\epsilon \sim \mathcal{N}(0, \sigma_\epsilon)$. This can be written in terms of the measurement equation $\kappa y_{ij} = \varrho(x_i, t_j) + \epsilon$, where κ is the inverse of the amplification factor. The likelihood $P(\mathbf{y}|\mathbf{f}, \sigma_\epsilon, \kappa)$ satisfies

$$\begin{aligned} \log P(\mathbf{y}|\mathbf{f}, \sigma_\epsilon, \kappa) &= -\frac{1}{2\sigma_\epsilon^2} \sum_{i=1}^n \sum_{j=1}^t (\varrho(x_i, t_j; \mathbf{f}) - \kappa y_{ij}) \\ &\quad - \frac{n}{2} \log(2\pi\sigma_\epsilon^2), \end{aligned} \quad (13)$$

where we made explicit that ϱ depends on \mathbf{f} , i.e., the GP evaluated at the positions x_i , $i = 1, \dots, n$. Under the GP assumption, the prior probability $P(\mathbf{f}|m, \sigma_f, l)$ is multivariate normal $\mathcal{N}(m, \mathbf{K})$ with mean m and covariance matrix $\mathbf{K}(\sigma_f, l)$ induced by the kernel. For the hierarchical parameters $(m, \sigma_\epsilon, \kappa, \sigma_f, l) =: \theta$ we assume a scaled sigmoid Gaussian prior $P(m, \sigma_\epsilon, \kappa, \sigma_f, l)$ such that

$$\theta = \theta_{\min} + \frac{(\theta_{\max} - \theta_{\min})}{1 + \exp(-\xi)}, \quad \xi \sim \mathcal{N}(\mu_\xi, \mathbb{1}\sigma_\xi), \quad (14)$$

where $\theta_{\min} := (m_{\min}, \sigma_{\epsilon\min}, \kappa_{\min}, \sigma_{f\min}, l_{\min})$, $\theta_{\max} := (m_{\max}, \sigma_{\epsilon\max}, \kappa_{\max}, \sigma_{f\max}, l_{\max})$, and (μ_ξ, σ_ξ) are referred to as hyperparameters. By virtue of the Bayes theorem the joint posterior probability for θ and \mathbf{f}

$$\begin{aligned} P(\mathbf{f}, m, \sigma_\epsilon, \kappa, \sigma_f, l|\mathbf{y}) &\propto P(\mathbf{y}|\mathbf{f}, \sigma_\epsilon, \kappa) \\ &\quad P(\mathbf{f}|m, \sigma_f, l)P(m)P(\sigma_\epsilon)P(\kappa)P(\sigma_f)P(l), \end{aligned} \quad (15)$$

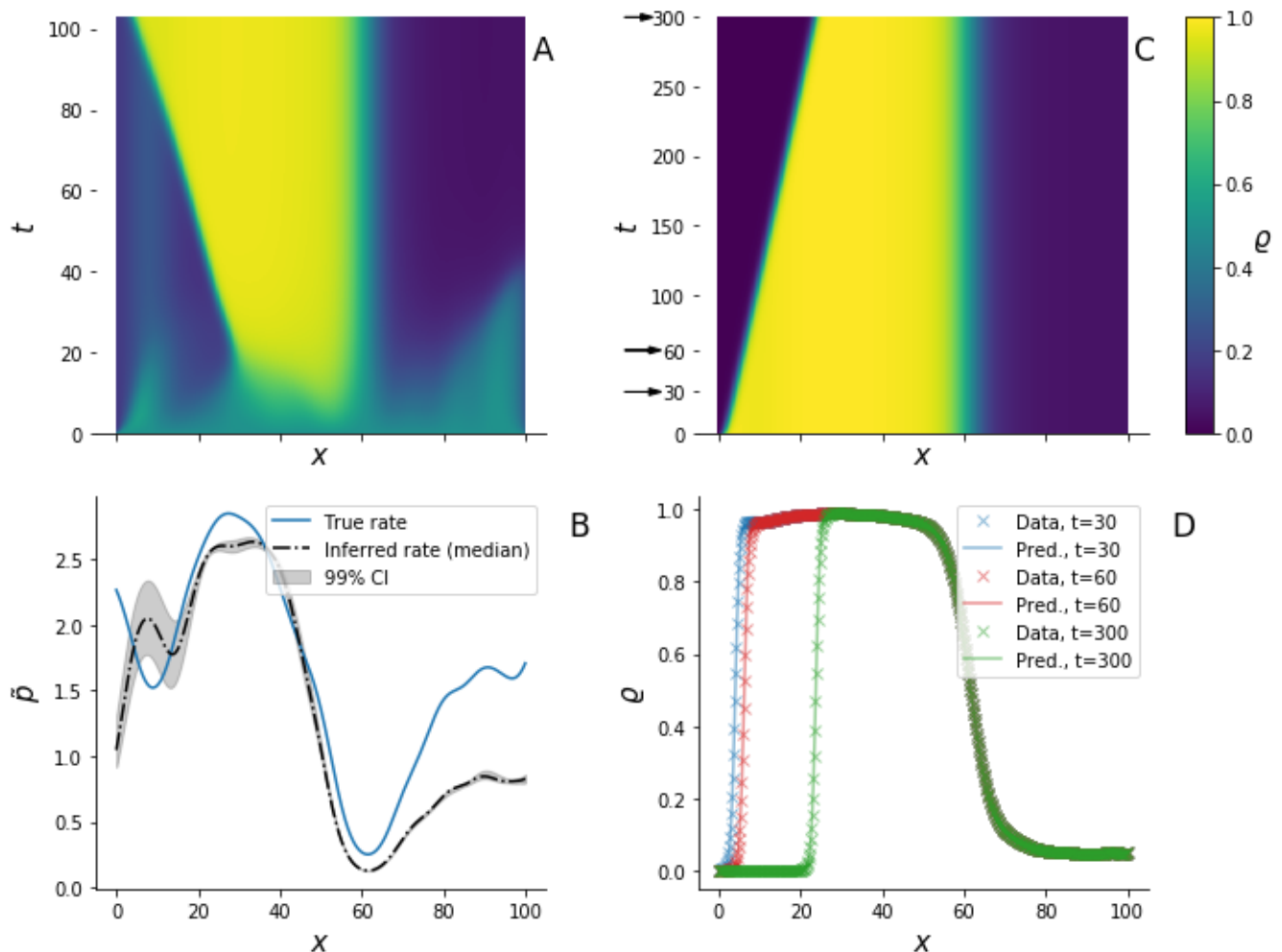


FIG. 2. Simulation study. A) A non-equilibrium stationary state (NESS) of profile $\rho^*(x)$ is obtained integrating the hydrodynamic TASEP with open boundaries, initial density profile $\rho(x, 0) = 0.5 \forall x \in [0, L]$, and chosen rate profile (solid line in (B)). B) True rate profile (solid line) and inferred rate profile (dash-dot line); the shaded area is 99% credible interval (CI). C) Integrating the same dynamics with initial profile $\rho^*(x)$ and no-influx boundary conditions show that the density decreases in proximity of the left-boundary, similar to ChIP-seq readings followed by Trp treatment; the density profiles corresponding to times 30, 60, and 300 and used for inference are marked by arrows. D) The posterior predictive samples (solid lines) are in excellent agreement with the extracted density profiles (cross markers).

which we draw random samples from by Markov chain Monte Carlo (MCMC) sampling scheme, more specifically block Gibbs sampling with elliptical slice sampling at each block [40, 41] (Appendix C). Evaluating the likelihood also requires computing ρ from equation (11) with initial condition $\rho(x, 0) = \kappa y^*(x), \forall x \in [0, L]$.

III. RESULTS

We first consider simulated data from a given profile of length $L = 100$ obtained from GP draws with parameters $(l, \sigma_f, m, \tilde{\rho}_{\max}) = (7.32, 0.67, 0.29, 3)$. We integrate the dynamics with NESS initial profile and no-influx boundary conditions, and extract density profiles y at times $(t_1, t_2, t_3) = (30, 60, 300)$ (Fig. 2). We set the hy-

perparameters $\theta_{\min}, \theta_{\max}$, and (μ_ξ, σ_ξ) to $(0, 0, 0.8, 0, 0)$, $(2, 10, 1.2, 1, 10)$, and $(0, 1)$, respectively. With these settings and data, we generated 3×10^3 MCMC samples targeting the posterior (15), discarding the first 2×10^3 as burn-in. The inferred rate profile (posterior median) approaches the true $\tilde{\rho}(x)$, thus demonstrating that the fitting procedure is able to capture the major features of the generative model (Fig. 2 C). The predicted transient density profiles are in excellent agreement with the input data (Fig. 2 D).

Applying this method to real-world data requires setting the value of $\tilde{\rho}_{\max}$ to an upper limit of prior expectations on the elongation rate. As this has been estimated at around 2×10^3 Nt/min in previous studies [17], we set $\tilde{\rho}_{\max} = 6 \times 10^3$ Nt/min as an arguably safe upper bound. Literature results can be also used to set tight bounds

on the prior for κ , which regularises the estimation problem [11]. From cultured human cell lines, the total number P of bound PolII molecules per cell is estimated to be between $P_{\min} = 11 \times 10^5$ and $P_{\max} = 18 \times 10^5$ [42]. This is related to the total number Y of ChIP-seq counts by $P = \kappa Y$. Based on these heuristic considerations, we set $\kappa_{\min} = P_{\min}/Y$ and $\kappa_{\max} = P_{\max}/Y$. All remaining hyperparameters were set identical to the previous simulation experiment.

The results from different genes show a variety of rate profiles which share similar patterns (Fig. 3). The most important observation is that rates vary strongly with the genomic position. In order to look for average patterns, it is desirable to aggregate data from all genes. As genes have different lengths (which in our sample range from 16,680 to 59,880 Nts), we stretch all the rate profiles in the region from TSS+1000 to TES-1000 Nts to the same support length and then average over the genes at each position. This yields the summaries illustrated in Fig. 4 which we refer to as *metagene* rates and are akin to the so-called metagene profiles [43]. Rates are typically lower near the TSS than in the gene body, where elongation approaches its highest rate. The behaviour in proximity of the TES is less definite, with rates varying several fold among the different genes. At the TSS the rate typically dips down consistently with the presence of obstacles that hinder the transport of PolII. Further downstream in the gene body the rate increases to its highest average value. While the dip is evident in both Spt5 and PolII results, it is worth noting that upstream the TSS the inferred rate is higher from PolII data than that from Spt5. We argue that this difference is due to the fact the former also include poised PolIIs which are not strongly bound to the template and can quickly move towards the TSS before being engaged in transcription. A by-product of the fitting procedure is the estimate of the occupation density $\rho(x, t) = \kappa y(x, t)$, as illustrated in Fig. 2 D for the simulation experiment and Figs. 5, S2, S3, and S4 for selected genes. The predicted densities are typically very low (total expected number of PolIIs in a gene is in the order of 10^{-1}), thus suggesting that crowding and congestion of PolIIs might not play an important role in gene expression.

IV. DISCUSSION

We developed a general Bayesian framework to study the dynamics of a one-dimensional transport model given time-resolved density profiles. The general problem addressed here is the identification of the PDE parameters that best describe data as a subset of the true PDE solution (see, e.g., [41, 44–46] and references therein). We focused on the hydrodynamic TASEP with smoothly-varying jump rates (which are the parameters to be inferred) as a paradigmatic and well-characterised model of transport. By means of its application to ChIP-seq time-course data, we inferred the rate of PolII elonga-

tion as a function of the genomic position in selected genes. This rate is not constant but varies within the gene body. It typically dips down nearby the TSS, confirming widespread pausing in this region, while in the bulk the rate also varies between genes.

The inference here is complicated by the high dimensionality of the parameter space. We addressed this by assuming a Gaussian process latent prior for the jump-rate profile and using elliptic slice sampling as an appropriate MCMC algorithm.

The study of these molecular dynamics is subject to limitations. While ChIP-seq is a widely-used assay to quantify the abundances of DNA-bound PolII, studies suggest that it might be subject to technical issues [47]. Further, the transcription of mRNA is a very complex process and it may be interesting to include features not encoded in the model used for this study. Further TASEP variants, such as those incorporating non-Markovian jump dynamics or Langmuir kinetics [48–50], are relevant for the modelling of PolII recycling and its early detachment from DNA [51, 52]. Potential extensions also include estimation of the parameters that encode the system’s size and asymmetry (a and b , respectively) and the boundary values. Nevertheless, including more features arguably comes at the cost of increased computational burden and decreased tractability. Conversely, the chosen TASEP with smoothly-varying jump rates is simple yet able to reveal PolII elongation slowing down and speeding up at certain genomic locations. Due to its generality, our approach also serves as a template for future studies seeking to shed light on complex transport phenomena.

MATERIALS AND METHODS

Spt5 and PolII ChIP-seq data mapped to the hg19 University of California at Santa Cruz human genome were downloaded from Gene Expression Omnibus (GEO, <http://www.ncbi.nlm.nih.gov/geo>), accession number GSE117006. We filtered the list of genes from the reference genome to only contain those with unique gene symbols on chromosomes 1–22 and X, thus excluding alternatively spliced genes. Hg19 gene coordinates were flanked 500 Nts upstream the TSS in order to include poised PolII. The 20 non-overlapping genes with the highest coverage of Spt5 ChIP-seq reads were selected. All simulation codes are written in Python (v3.7.1), with the PDE solver using Numba JIT compiler (v0.41.0) [53] (<https://github.com/mcavallaro/dTASEP-fit>).

ACKNOWLEDGMENTS

This research utilised WISB computational facilities (grant ref: BB/M017982/1) funded under the UK Research Councils’ Synthetic Biology for Growth

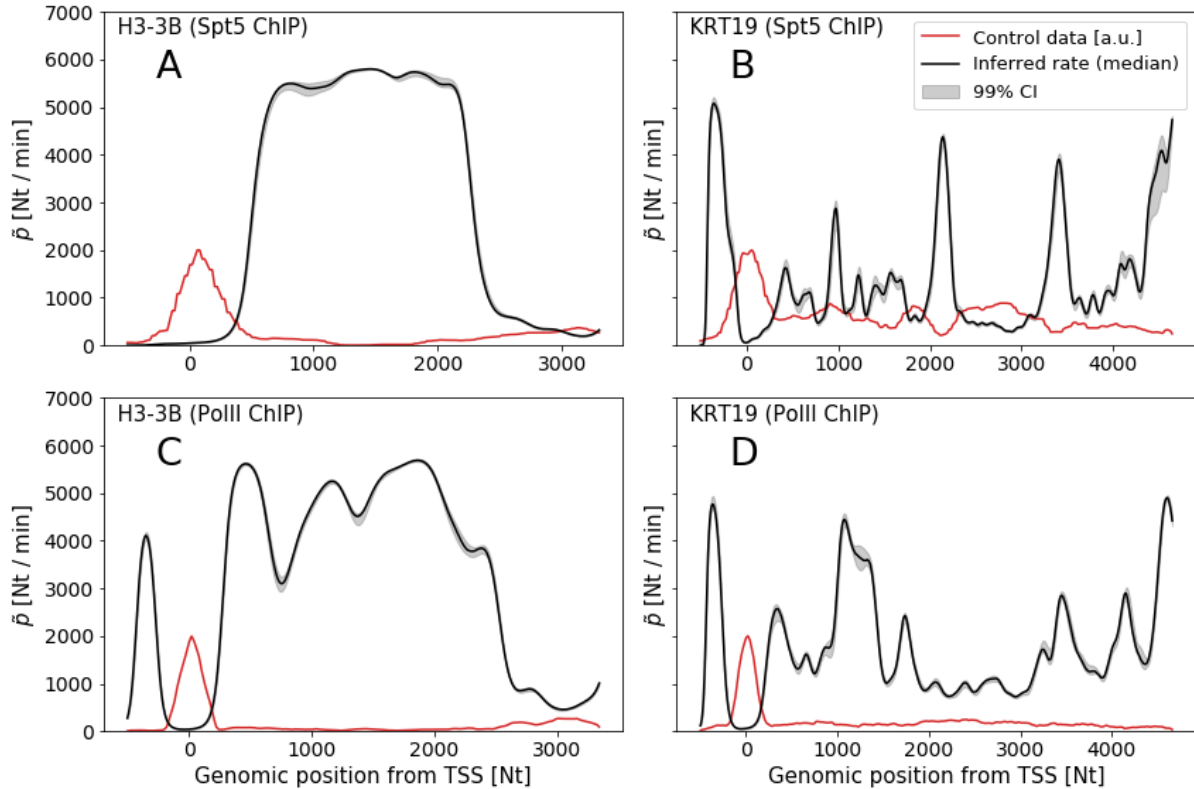


FIG. 3. Inferred rate profiles from Spt5 ChIP-Seq (A-B) and PolII ChIP-Seq (C-D) for genes H3-B3 (A-C) and KRT19 (B-D) (black lines are posterior medians, shaded area are 99% credible intervals), with the latter gene showing a distinctive jagged profiles. Both genes show the lowest rates in proximity of the transcription starting site (TSS). Red lines are unperturbed ChIP-seq signals in arbitrary units (a.u.).

programme. RD is funded by EPSRC (grant nos. EP/V025899/1, EP/T017112/1) and NERC (grant no. NE/T00973X/1). MC acknowledges support from Matt J. Keeling and Health Data Research UK, which is funded by the UK Medical Research Council, EPSRC, Economic and Social Research Council, Department of Health and Social Care (England), Chief Scientist Office of the Scottish Government Health and Social Care Directorates, Health and Social Care Research and Development Division (Welsh Government), Public Health Agency (Northern Ireland), British Heart Foundation

and the Wellcome Trust. We thank Carlo Albert and Jie Zhang for valuable comments.

AUTHOR CONTRIBUTIONS

Conceptualization MC DH RD; Data curation MC DH; Formal analysis MC RD; Investigation MC; Software MC YW RD; Writing – original draft MC; Writing – review & editing MC DH RD.

-
- [1] B. Munsky, G. Neuert, and A. van Oudenaarden, *Science* **336**, 183 (2012).
- [2] T. Rajala, A. Häkkinen, S. Healy, O. Yli-Harja, and A. S. Ribeiro, *PLOS Computational Biology* **6**, 1 (2010).
- [3] I. Jonkers and J. T. Lis, *Nature Reviews Molecular Cell Biology* **16**, 167 (2015).
- [4] A. Mayer, H. M. Landry, and L. S. Churchman, *Current Opinion in Cell Biology* **46**, 72 (2017).
- [5] K. Adelman and J. T. Lis, *Nature reviews. Genetics* **13**, 720 (2012).
- [6] X. Liu, W. L. Kraus, and X. Bai, *Trends in Biochemical Sciences* **40**, 516 (2015).
- [7] F. Spitzer, *Advances in Mathematics* **5**, 246 (1970).
- [8] A. Benassi and J.-P. Fouque, *The Annals of Probability* **15**, 546 (1987).
- [9] R. J. Harris and R. B. Stinchcombe, *Physical Review E - Statistical, Nonlinear, and Soft Matter Physics* **70**, 016108 (2004).
- [10] R. B. Stinchcombe and S. L. De Queiroz, *Physical Review E - Statistical, Nonlinear, and Soft Matter Physics* **83**, 1 (2011).

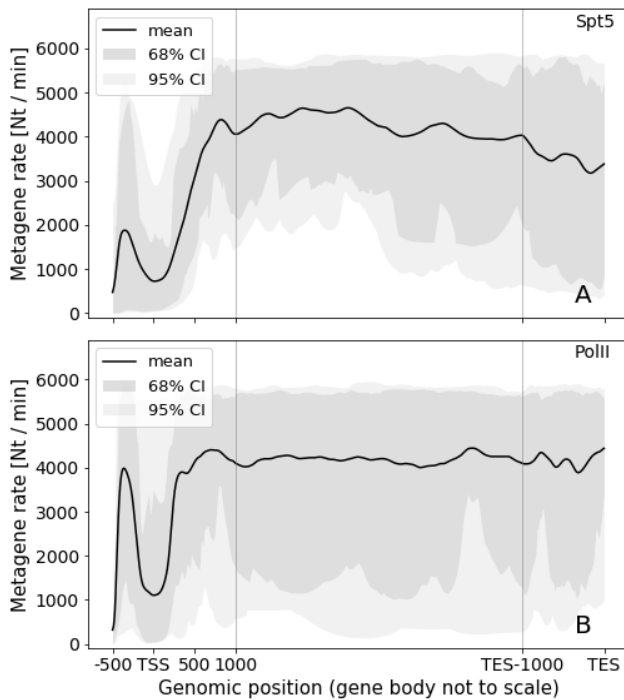


FIG. 4. Metagene rates from PolII ChIP-seq (A) and Spt5 ChIP-seq (B) data. By construction, the metagene analysis conserves the length scale only in proximity of TSS and TES. Upstream of TSS the Spt5 ChIP-seq yields lower average rate than PolII ChIP-seq, as this assay does not detect PolII poised to move downstream.

- [11] C. E. Rasmussen and C. K. I. Williams, *Gaussian processes for machine learning* (MIT Press, 2006) p. 248.
- [12] B. Hu, N. Petela, A. Kurze, K.-L. Chan, C. Chapard, and K. Nasmyth, *Nucleic Acids Research*, gkv670 (2015).
- [13] T. Nojima, T. Gomes, A. R. F. Grosso, H. Kimura, M. J. Dye, S. Dhir, M. Carmo-Fonseca, and N. J. Proudfoot, *Cell* **161**, 526 (2015).
- [14] L. J. Core, J. J. Waterfall, and J. T. Lis, *Science* **322**, 1845 (2008).
- [15] H. Kwak, N. J. Fuda, L. J. Core, and J. T. Lis, *Science* **339**, 950 (2013).
- [16] J. Zhang, M. Cavallaro, and D. Hebenstreit, *Cell Reports Methods* (2021), 10.1101/461442.
- [17] I. Jonkers, H. Kwak, and J. T. Lis, *eLife* **2014**, 1 (2014).
- [18] B. Erickson, R. M. Sheridan, M. Cortazar, and D. L. Bentley, *Genes and Development* **32**, 1215 (2018).
- [19] T. Chou, K. Mallick, and R. K. P. Zia, *Reports on Progress in Physics* **74**, 116601 (2011).
- [20] J. Cholewa-Waclaw, R. Shah, S. Webb, K. Chhatbar, B. Ramsahoye, O. Pusch, M. Yu, P. Greulich, B. Waclaw, and A. P. Bird, *Proceedings of the National Academy of Sciences of the United States of America* **116**, 14995 (2019).
- [21] C. T. MacDonald, J. H. Gibbs, and A. C. Pipkin, *Biopolymers* **6**, 1 (1968).
- [22] R. K. P. Zia, J. J. Dong, and B. Schmittmann, *Journal of Statistical Physics* **144**, 405 (2011).
- [23] J. Szavits-Nossan, L. Ciandrini, and M. C. Romano, *Physical Review Letters* **120**, 128101 (2018).
- [24] D. D. Erdmann-Pham, K. Dao Duc, and Y. S. Song, *Cell Systems* **10**, 183 (2020).
- [25] R. Lipowsky, S. Klumpp, and T. M. Nieuwenhuizen, *Physical Review Letters* **87**, 108101 (2001).
- [26] D. Chowdhury, L. Santen, and A. Schadschneider, *Physics Reports* **329**, 199 (2000).
- [27] B. Waclaw, J. Cholewa-Waclaw, and P. Greulich, *Journal of Physics A: Mathematical and Theoretical* **52**, 065002 (2019).
- [28] M. Kardar, G. Parisi, and Y. C. Zhang, *Physical Review Letters* **56**, 889 (1986).
- [29] L. Bertini and G. Giacomin, *Communications in Mathematical Physics* **183**, 571 (1997).
- [30] B. Derrida, M. R. Evans, V. Hakim, and V. Pasquier, *Journal of Physics A: Mathematical and General* **26**, 1493 (1993).
- [31] C. wa Maina, A. Honkela, F. Matarese, K. Grote, H. G. Stunnenberg, G. Reid, N. D. Lawrence, and M. Rattray, *PLoS Computational Biology* **10**, 1 (2014).
- [32] A. Honkela, J. Peltonen, H. Topa, I. Charapitsa, F. Matarese, K. Grote, H. G. Stunnenberg, G. Reid, N. D. Lawrence, and M. Rattray, *Proceedings of the National Academy of Sciences* **112**, 13115 (2015).
- [33] Z. Cao, T. Filatova, D. A. Oyarzún, and R. Grima, *Biophysical Journal* **119**, 1002 (2020).
- [34] A. Lazarescu, *Journal of Physics A: Mathematical and Theoretical* **48**, 503001 (2015).
- [35] E. Nudler, A. Mustaev, A. Goldfarb, and E. Lukhtanov, *Cell* **89**, 33 (1997).
- [36] F. Jülicher and R. Bruinsma, *Biophysical Journal* **74**, 1169 (1998).
- [37] E. Hopf, *Communications on Pure and Applied Mathematics* **3**, 201 (1950).
- [38] J. D. Cole, *Quarterly of Applied Mathematics* **9**, 225 (1951).
- [39] A. Gelman, J. B. Carlin, H. S. Stern, D. B. Dunson, A. Vehtari, and D. B. Rubin, *Bayesian data analysis* (CRC press, 2013).
- [40] I. Murray, R. Adams, and D. MacKay, in *Proceedings of the thirteenth international conference on artificial intelligence and statistics* (JMLR Workshop and Conference Proceedings, 2010) pp. 541–548.
- [41] M. Tegnér and S. Roberts, arXiv preprint arXiv:1901.06021 (2019).
- [42] H. Kimura, Y. Tao, R. G. Roeder, and P. R. Cook, *Molecular and cellular biology* **19**, 5383 (1999).
- [43] C. Joly Beuparlant, F. C. Lamaze, A. Deschênes, R. Samb, A. Lemaçon, P. Belleau, S. Bilodeau, and A. Droit, *PLOS Computational Biology* **12**, 1 (2016).
- [44] S. H. Rudy, S. L. Brunton, J. L. Proctor, and J. N. Kutz, *Science Advances* **3**, e1602614 (2017).
- [45] M. Raissi, P. Perdikaris, and G. Karniadakis, *Journal of Computational Physics* **378**, 686 (2019).
- [46] J. Berg and K. Nyström, *Journal of Computational Physics* **384**, 239 (2019).
- [47] P. J. Park, *Nature Reviews. Genetics* **10**, 669 (2009).
- [48] A. Parmeggiani, T. Franosch, and E. Frey, *Physical Review E* **70**, 046101 (2004).
- [49] D. Khoromskaia, R. J. Harris, and S. Grosskinsky, *Journal of Statistical Mechanics: Theory and Experiment* **2014**, P12013 (2014).
- [50] R. J. Concannon and R. A. Blythe, *Physical Review Letters* **112**, 050603 (2014).

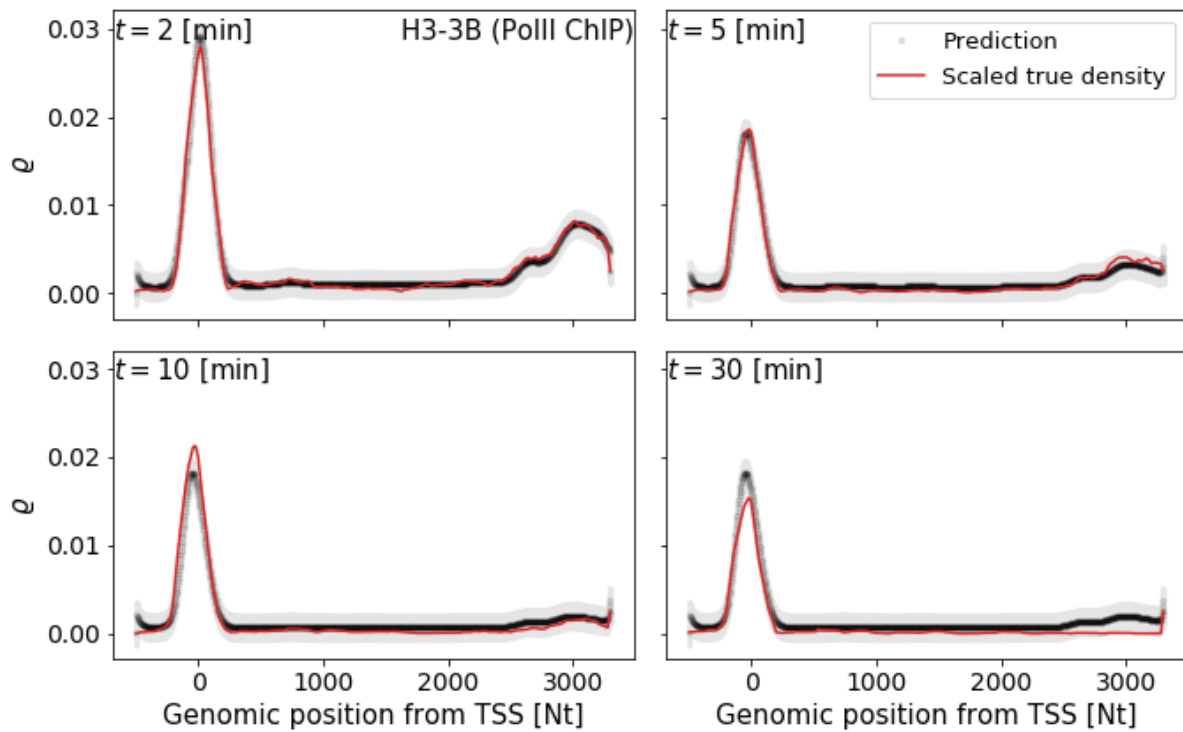


FIG. 5. Predicted density profiles for gene H3-3B from Spt5 ChIP-seq 2, 5, 10, and 20 minutes after Trp treatment as samples from posterior predictive distribution. Grey area is 95% credible interval due to noise model.

- [51] B. Steurer, R. C. Janssens, B. Geverts, M. E. Geijer, F. Wienholz, A. F. Theil, J. Chang, S. Dealy, J. Pothof, W. A. van Cappellen, A. B. Houtsmuller, and J. A. Martejijn, *Proceedings of the National Academy of Sciences of the United States of America* **115**, E4368 (2018).
- [52] M. Cavallaro, M. D. Walsh, M. Jones, J. Teahan, S. Tiberi, B. Finkenstädt, and D. Hebenstreit, *Genome Biology* **22**, 56 (2021).
- [53] S. K. Lam, A. Pitrou, and S. Seibert, in *Proceedings of the Second Workshop on the LLVM Compiler Infrastructure in HPC - LLVM '15* (ACM Press, New York, New York, USA, 2015) pp. 1–6.

Appendix A: Cole-Hopf transform

Let us define a “height” variable $h(x, t)$ as follows:

$$\varrho(x, t) =: \frac{\partial}{\partial x} h(x, t) + \frac{1}{2}. \quad (\text{A1})$$

Substituting this into equation (11) of the main text yields

$$\frac{\partial}{\partial t} \frac{\partial}{\partial x} h(x, t) = -\frac{\partial}{\partial x} \left\{ \lambda(x) \left(\frac{\partial}{\partial x} h(x, t) + \frac{1}{2} \right) \left(\frac{1}{2} - \frac{\partial}{\partial x} h(x, t) \right) - \nu(x) \frac{\partial^2}{\partial x^2} h(x, t) \right\} \quad (\text{A2})$$

and integrating over x gives

$$\frac{\partial}{\partial t} h(x, t) = -\lambda(x) \left(\frac{\partial}{\partial x} h(x, t) + \frac{1}{2} \right) \left(\frac{1}{2} - \frac{\partial}{\partial x} h(x, t) \right) + \nu(x) \frac{\partial^2}{\partial x^2} h(x, t) + f(t), \quad (\text{A3})$$

which is a noiseless version of the paradigmatic growth model studied by Kardar, Parisi, and Zhang [28] up to an arbitrary integration function $f(t)$ constant in x .

This equation is linearised by means of the transformation

$$h(x, t) =: \frac{a}{2} \frac{1+b}{1-b} \ln u(x, t) + F(t), \quad (\text{A4})$$

which obviously implies

$$\frac{\partial}{\partial x} h(x, t) = \frac{a}{2} \frac{1+b}{1-b} \frac{u_x(x, t)}{u(x, t)}. \quad (\text{A5})$$

We refer to $u(x, t)$ as the “field”.

Merely substituting (A4) into equation (A3) and choosing $F(t)$ to remove the term $f(t)$ yields

$$\frac{a}{2} \frac{1+b}{1-b} \frac{u_t(x, t)}{u(x, t)} = -\left\{ \lambda(x) \left[\frac{1}{4} - \left(\frac{a}{2} \frac{1+b}{1-b} \frac{u_x(x, t)}{u(x, t)} \right)^2 \right] - \nu(x) \frac{a}{2} \frac{1+b}{1-b} \frac{\partial}{\partial x} \frac{u_x(x, t)}{u(x, t)} \right\}, \quad (\text{A6})$$

$$\frac{a}{2} \frac{1+b}{1-b} \frac{u_t(x, t)}{u(x, t)} = -a\tilde{p}(x) \left\{ \left[\frac{(1-b)}{4} - \frac{a^2}{4} \frac{(1+b)^2}{(1-b)} \frac{(u_x(x, t))^2}{u^2(x, t)} \right] - \frac{a^2}{4} \frac{(1+b)^2}{1-b} \left(\frac{u_{xx}(x, t)}{u(x, t)} - \frac{(u_x(x, t))^2}{u^2(x, t)} \right) \right\}, \quad (\text{A7})$$

$$\frac{1}{2} \frac{1+b}{1-b} \frac{u_t(x, t)}{u(x, t)} = -\tilde{p}(x) \left\{ \frac{(1-b)}{4} - \frac{a^2}{4} \frac{(1+b)^2}{(1-b)} \frac{(u_x(x, t))^2}{u^2(x, t)} - \frac{a^2}{4} \frac{(1+b)^2}{1-b} \frac{u_{xx}(x, t)}{u(x, t)} + \frac{a^2}{4} \frac{(1+b)^2}{1-b} \frac{(u_x(x, t))^2}{u^2(x, t)} \right\}, \quad (\text{A8})$$

$$\frac{\partial}{\partial t} u(x, t) = \frac{\tilde{p}(x)}{2} \left\{ a^2 (1+b) \frac{\partial^2}{\partial x^2} u(x, t) - \frac{(1-b)^2}{1+b} u(x, t) \right\}, \quad (\text{A9})$$

which, for the totally asymmetric case $b = 0$, can be simplified to

$$\frac{\partial}{\partial t} u(x, t) = \frac{\tilde{p}(x)}{2} \left\{ a^2 \frac{\partial^2}{\partial x^2} u(x, t) - u(x, t) \right\}. \quad (\text{A10})$$

If $\tilde{p}(x) = p$, it is possible to incorporate a term $ap(1-b)t/4$ in $F(t)$ to eliminate the second term on the right-hand side of equation (A10), thus further simplifying it to a diffusion equation.

Equation (A9) preserves the full dynamics of equation (11) of the main text and is linear, thus is easier to treat numerically than the latter. In the next sections we elucidate the numerical scheme for its integration for $b = 0$.

We impose Dirichlet boundary conditions for $\varrho(x, t)$ at $x = 0$ and $x = L$, i.e.,

$$\begin{aligned} \varrho(0, t) &= \varrho_{\text{left}}(t), \\ \varrho(L, t) &= \varrho_{\text{right}}(t), \end{aligned} \quad (\text{A11})$$

$\forall t > 0$, which implies Neumann conditions for the height $h(x, t)$:

$$\begin{aligned} h_x(x, t)|_{x=0} &= \varrho_{\text{left}}(t) - \frac{1}{2}, \\ h_x(x, t)|_{x=L} &= \varrho_{\text{right}}(t) - \frac{1}{2}, \end{aligned} \quad (\text{A12})$$

and Robin (mixed) boundary conditions for the field $u(x, t)$:

$$(2\varrho_{\text{left}}(t) - 1)u(0, t)/a - u_x(x, t)|_{x=0} = 0, \quad (\text{A13})$$

$$(2\varrho_{\text{right}}(t) - 1)u(L, t)/a - u_x(x, t)|_{x=L} = 0. \quad (\text{A14})$$

Appendix B: Numerical integration

The solution u^* of equation (A10) at the coordinates $(i \Delta x, j \Delta t)$ is approximated by $U_{j,i}$ ($j = 0, 1, \dots, T$ and $i = 0, 1, \dots, N$ with $N = L/\Delta x$) which is computed using the forward Euler explicit iterative procedure

$$U_{j+1,i} = U_{j,i} + P_i \left[a^2 \frac{U_{j,i-1} - 2U_{j,i} + U_{j,i+1}}{\Delta x^2} - U_{j,i} \right] \Delta t, \quad (\text{B1})$$

where $P_i = \tilde{p}(i \Delta x)$. The approximated density $\rho_{j,i} \approx \varrho(i \Delta x, j \Delta t)$ is recovered from $U_{j,i}$ by means of the transformation

$$\begin{aligned} H_{j,i} &= \frac{a}{2} \ln U_{j,i}, \\ \rho_{j,i} &= \frac{1}{2} + \frac{H_{j,i+1} - H_{j,i-1}}{2\Delta x}. \end{aligned} \quad (\text{B2})$$

Initial values $U_{0,i}$, $i = 0, 1, \dots, N$, are obtained by means of the discrete Cole-Hopf transform

$$U_{j,i} = \exp \left(\sum_{k=0}^i \frac{1}{a} (2\rho_{j,k} - 1) \Delta x \right), \quad (\text{B3})$$

at $j = 0$ and given $\rho_{0,i}$. We deal with the boundary conditions by introducing ghost grid points ($j, -1$) and ($j, N+1$), with $j = 0, 1, 2, \dots, T$), where the values of U are determined according to the procedure detailed below.

We use a central difference formula to approximate the derivatives

$$u_x|_{x=0}(x, t) \approx \frac{U_{j,1} - U_{j,-1}}{2\Delta x}, \quad (\text{B4})$$

$$u_x|_{x=L}(x, t) \approx \frac{U_{j,N+1} - U_{j,N-1}}{2\Delta x}, \quad (\text{B5})$$

while $u(0, t) \approx U_{j,1}$ and $u(L, t) \approx U_{j,N}$. Substituting into equations (A13)–(A14):

$$U_{j,-1} \approx U_{j,1} - 2\Delta x [2\rho_{j,0} - 1] \frac{1}{a} U_{j,0}, \quad (\text{B6})$$

$$U_{j,N+1} \approx +2\Delta x [2\rho_{j,N} - 1] \frac{1}{a} U_{j,N} + U_{j,N-1}. \quad (\text{B7})$$

The off-grid values $U_{j,-1}$ and $U_{j,N+1}$ correspond to the ghost grid points and are eliminated by substitution from the recursion relations (B1) at $i = 0$ and $i = N$, which we write for convenience:

$$U_{j+1,0} = U_{j,0} + P_0 \left[a^2 \frac{U_{j,-1} - 2U_{j,0} + U_{j,1}}{\Delta x^2} - U_{j,0} \right] \Delta t, \quad (\text{B8})$$

$$U_{j+1,N} = U_{j,N} + P_N \left[a^2 \frac{U_{j,N-1} - 2U_{j,N} + U_{j,N+1}}{\Delta x^2} - U_{j,N} \right] \Delta t. \quad (\text{B9})$$

The approximated second derivatives in the square brackets therefore are

$$\frac{U_{j,-1} - 2U_{j,0} + U_{j,1}}{\Delta x^2} = \frac{L_j U_{j,0} + 2U_{j,1}}{\Delta x^2}, \quad \text{with } L_j = -2 - 2[2\rho_{j,0} - 1] \Delta x \frac{1}{a}, \quad (\text{B10})$$

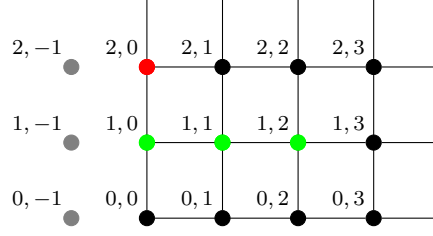


FIG. S1. Evaluation of the discretised field U at left-boundary grid nodes. The value at the red node is obtained from the values at the green nodes. Grey points are ghost grid nodes.

and

$$\frac{U_{j,N-1} - 2U_{j,N} + U_{j,N+1}}{\Delta x^2} = \frac{2U_{j,N-1} + R_j U_{j,N}}{\Delta x^2}, \quad \text{with } R_j = -2 + 2[2\rho_{j,N} - 1]\Delta x \frac{1}{a}, \quad (\text{B11})$$

for the left and the right boundaries, respectively.

The recruitment of new PolIII at the 5' end of the gene is arrested upon chemical perturbation of the promoters with Trp. This is modelled by assuming that a PolIII molecule at the leftmost site can leave its position, whilst no molecules can be injected. Therefore, in mean-field approximation, the average number of particles at the left boundary of the system obeys

$$\frac{d\phi_0(t)}{dt} = -p_0\phi_0(t)(1 - \phi_1(t)), \quad (\text{B12})$$

whose hydrodynamic limit is approximated by

$$\frac{\partial}{\partial t}\varrho(0,t) \approx -a\tilde{p}(0)\varrho(0,t)(1 - \varrho(0,t) - a\frac{\partial}{\partial x}\varrho(x,t)|_{x=0}^+). \quad (\text{B13})$$

$$(\text{B14})$$

with discretised iterative solution

$$\begin{aligned} \rho_{j+1,0} - \rho_{j,0} &= -\Delta t a P_0 \rho_{j,0} \left(1 - \rho_{j,0} - a \frac{\rho_{j,1} - \rho_{j,0}}{\Delta x} \right), \\ \rho_{0,0} &= \varrho_L(0), \\ \rho_{0,1} &= \varrho(\Delta x, 0). \end{aligned} \quad (\text{B15})$$

Using equations (B15) to iteratively update L_j in (B10) yields open boundary conditions, which are used in the simulation experiments.

Sequencing data shows that, at the beginning of the flanked region upstream of the TSS, expression is very low and thus signal will remain constantly close to zero during the time course. The reads downstream the TES are also assumed to be constant within measurement errors, given that the Trp perturbation at the TSS does not propagate up until the TES in the longest time course. Based on this, we set fixed left and right boundary conditions. The grid constants Δt and Δx are chosen such that $\Delta t/\Delta x^2 = 1/\tilde{p}_{\max}$, which guarantees numerical stability at each grid point provided that $\tilde{p}(x) < \tilde{p}_{\max} \forall x \in [0, L]$. The initial values over this grid at $j = 0$ are obtained from the binned read profile y^* by means of linear interpolation.

Appendix C: MCMC sampling

In equation (15) of the main text, the posterior probability $P(\mathbf{f}, m, \sigma_\epsilon, \kappa, \sigma_f, l | \mathbf{y})$ is expressed as proportional to the likelihood $P(\mathbf{y} | \mathbf{f}, \sigma_\epsilon, \kappa)$, multiplied by the latent GP prior $P(\mathbf{f} | m, \sigma_f, l)$ times the prior $P(m, \sigma_\epsilon, \kappa, \sigma_f, l)$. To sample from this posterior we used a blocked Gibbs sampling scheme where we recursively update the latent variable \mathbf{f} , the two covariance variables l, σ_f , and the three likelihood variables $m, \kappa, \sigma_\epsilon$, using the so-called elliptic slice sampler [40] for each block.

In order to update \mathbf{f} as a first block we parametrise the posterior such that m is absorbed into the likelihood, i.e.,

$$P(\mathbf{f}', m, \sigma_\epsilon, \kappa, \sigma_f, l | \mathbf{y}) \propto P(\mathbf{y} | \mathbf{f}', m, \sigma_\epsilon, \kappa) P(\mathbf{f}' | \sigma_f, l) P(m) P(\sigma_\epsilon) P(\kappa) P(\sigma_f) P(l), \quad (\text{C1})$$

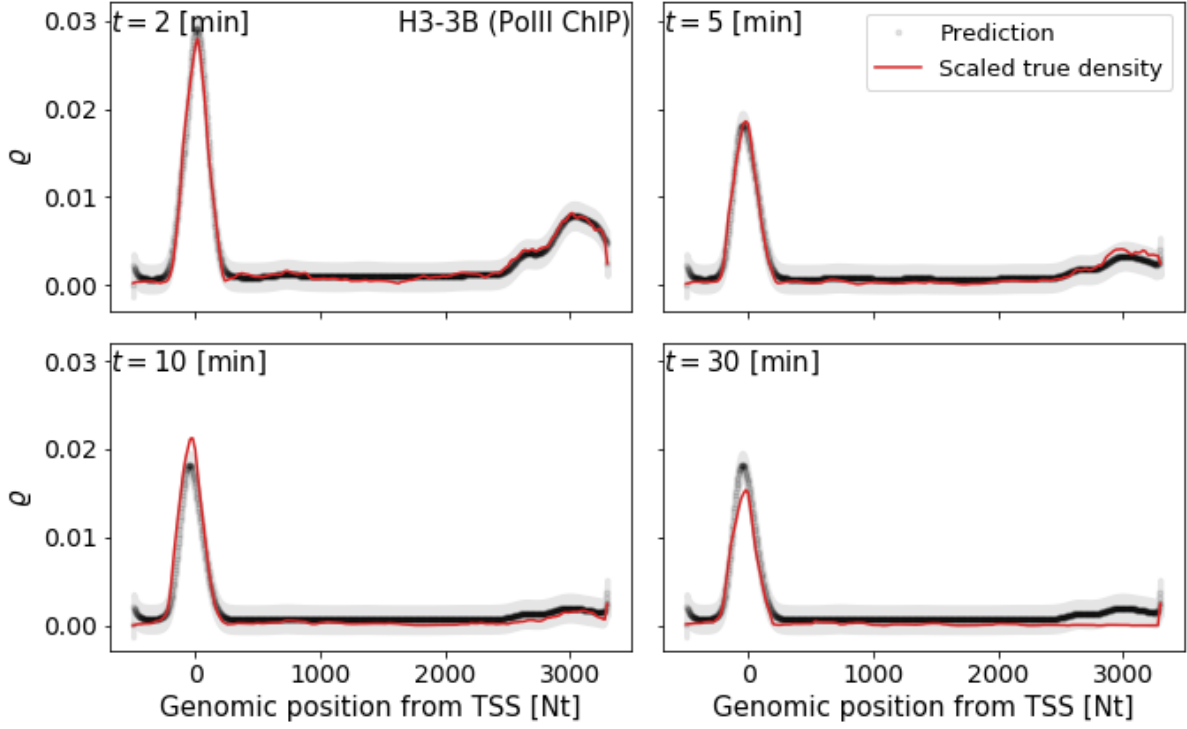


FIG. S2. Predicted density profiles for gene H3-3B from PolII ChIP-seq 2, 5, 10, and 20 minutes after Trp treatment. Markers are posterior predictive samples. Grey area is 95% credible interval due to noise model.

where $\mathbf{f}' = \mathbf{f} - m$, and sample from the unnormalised conditional $P(\mathbf{y}|\mathbf{f}', m, \sigma_\epsilon, \kappa)P(\mathbf{f}'|\sigma_f, l)$ with all hyperparameters $m, \sigma_\epsilon, \kappa, \sigma_f$, and l held fixed.

Updating the second block (l, σ_f) naively is difficult as this is strongly correlated with \mathbf{f} . Hence we adopt another parametrisation, which consists of expressing the multivariate Gaussian random variable \mathbf{f}' as the deterministic function of $\boldsymbol{\nu}$

$$\mathbf{f}'(\boldsymbol{\nu}, \sigma_f, l) = \mathbf{L}\boldsymbol{\nu}, \quad (\text{C2})$$

where $\mathbf{L}(\sigma_f, l)$ satisfies $\mathbf{L}\mathbf{L}^{-1} = \mathbf{K}(\sigma_f, l)$ (it can be computed from \mathbf{K} using a Cholesky decomposition) and $\boldsymbol{\nu} \sim \mathcal{N}(0, \mathbb{1})$ is independent of the other variables. This parametrisation incorporates all variables into the likelihood and results in the equivalent posterior

$$P(\boldsymbol{\nu}, m, \sigma_\epsilon, \kappa, \sigma_f, l|\mathbf{y}) \propto P(\mathbf{y}|\mathbf{f}'(\boldsymbol{\nu}, \sigma_f, l), m, \sigma_\epsilon, \kappa)P(\boldsymbol{\nu})P(m)P(\sigma_\epsilon)P(\kappa)P(\sigma_f)P(l). \quad (\text{C3})$$

For a given value of $(\mathbf{f}', l, \sigma_f)$, $\boldsymbol{\nu}$ is obtained as $\boldsymbol{\nu} = \mathbf{L}(\sigma_f, l)^{-1} \mathbf{f}'$. Hence with parameters \mathbf{f}', m, κ , and σ_ϵ held fixed, we update (σ_f, l) with a sample from the unnormalised conditional $P(\mathbf{y}|\mathbf{f}'(\boldsymbol{\nu}, \sigma_f, l), \kappa, \sigma_\epsilon)P(\sigma_f)P(l)$.

In the third step, given the values for \mathbf{f}', l , and σ_f , the likelihood hyperparameters m, σ_ϵ , and κ are updated by sampling from the unnormalised conditional $P(\mathbf{y}|\mathbf{f}', m, \sigma_\epsilon)P(m)P(\sigma_\epsilon)P(\kappa)$. We refer the reader to [41] for more details.

Appendix D: Supplemental figures

Figs. S2, S3, and S4 illustrate the posterior predictive samples and the scaled ChIP-seq reads.

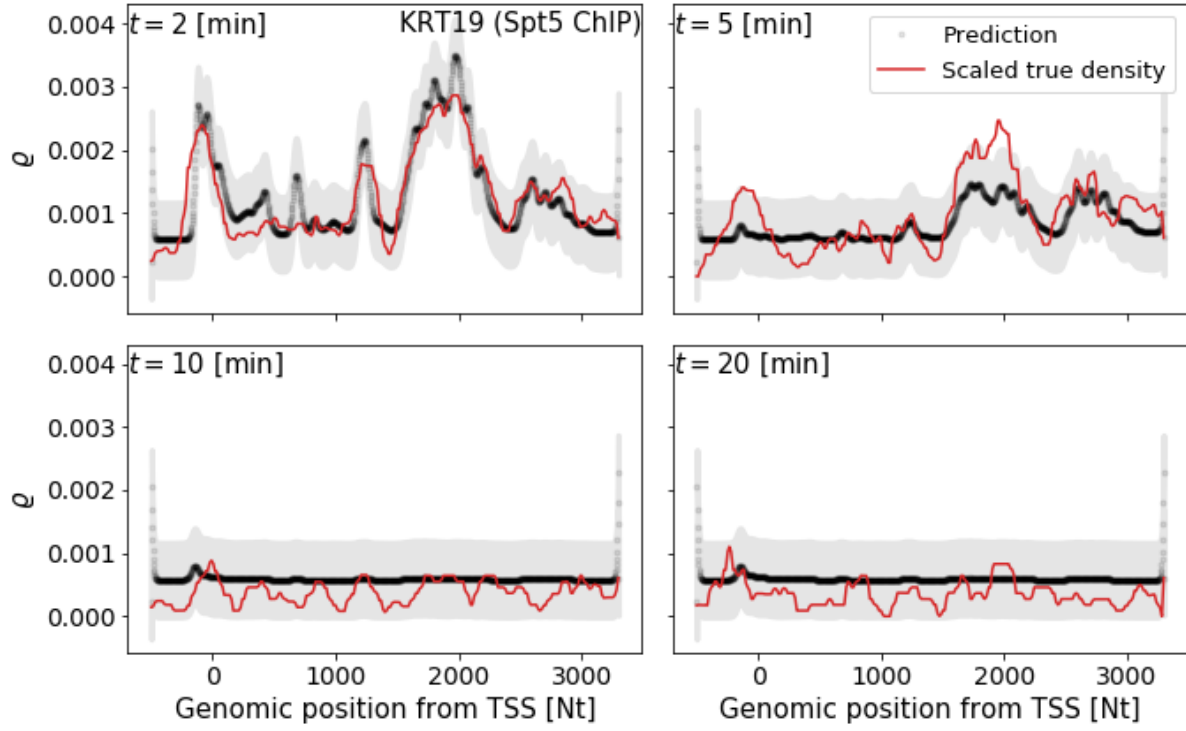


FIG. S3. Predicted density profiles for gene KRT19 from Spt5 ChIP-seq. Figure keys as in Fig. S2.

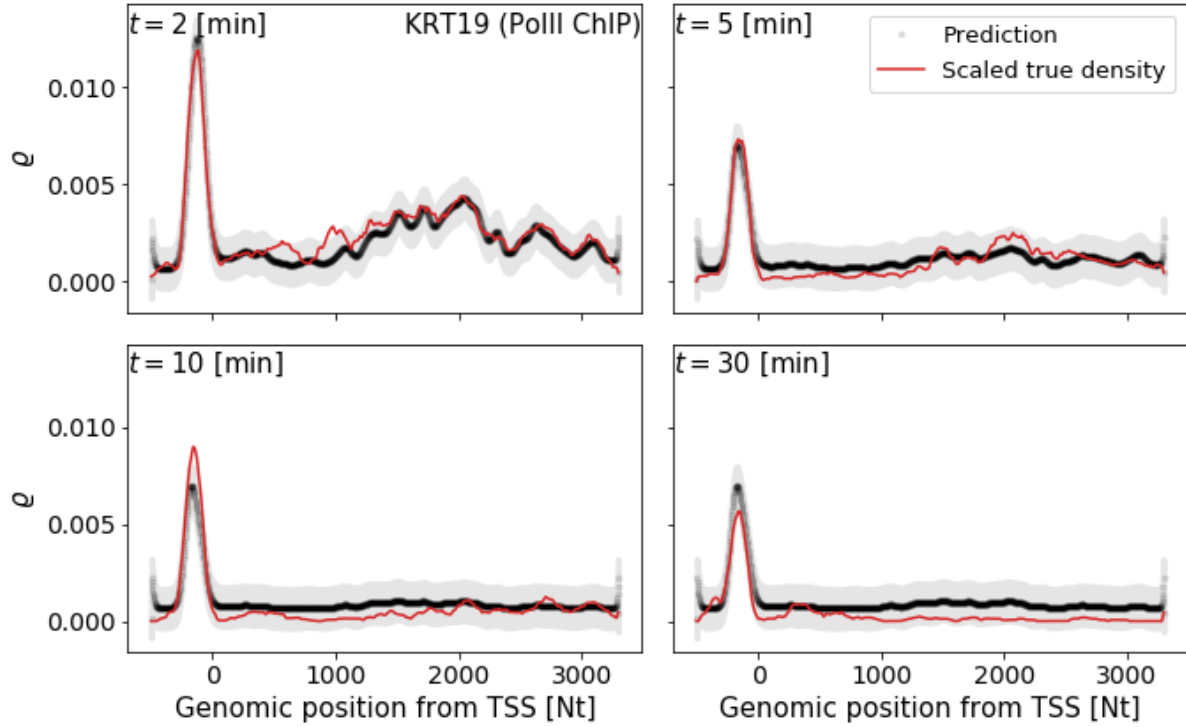


FIG. S4. Predicted density profiles for gene KRT19 from PolII ChIP-seq. Figure keys as in Fig. S2.